Radiocarbon, Vol 59, Nr 3, 2017, p 905–913 DOI:10.1017/RDC.2016.85
Selected Papers from the 2015 Radiocarbon Conference, Dakar, Senegal, 16–20 November 2015

RADIOCARBON ANALYSIS ON THE NEW AARAMS 1MV TANDETRON

Jesper Olsen[1*] • Dmitry Tikhomirov[1] • Claus Grosen[1] • Jan Heinemeier[1] • Matthias Klein[2]

[1]Aarhus AMS Centre (AARAMS), Department of Physics and Astronomy, Aarhus University, Ny Munkegade 120, DK-8000 Aarhus C, Denmark.
[2]High Voltage Engineering Europa (HVE), Amersfoort, The Netherlands.

ABSTRACT. We report here on the radiocarbon performance on the AARAMS HVE 1MV Tandetron. ^{14}C analysis is carried out in charge state 2+. We have avoided Li interference by appropriate settings of the high-energy electrostatic analyzer and the 30° second high-energy magnet. The ^{14}C machine background is determined using unprocessed graphite, which yielded 58,650 ± 2032 ^{14}C yr determined as the average and standard deviation of four measurements. International standards, which are used to monitor the long-term performance of the ^{14}C measurements, agree with the reported consensus values.

KEYWORDS: radiocarbon, AMS, dating.

INTRODUCTION

In November 2014, the Aarhus AMS Centre (AARAMS) received a compact 1MV multi-element accelerator mass spectrometry (AMS) system capable of analyzing ^{3}H, ^{10}Be, ^{14}C, ^{26}Al, ^{41}Ca, ^{129}I, ^{239}Pu, and ^{240}Pu from High Voltage Engineering Europa (HVE) (Klein et al. 2006, 2007). For a report on the acceptance tests of all isotopes, see Heinemeier et al. (2015) and Klein et al. (2014). This article reports on our progress in ^{14}C analysis.

DESCRIPTION OF THE AMS SYSTEM

A detailed description of the AARAMS AMS system has been given elsewhere (Klein et al. 2014). Here, we give a short summary with a focus on ^{14}C analysis (Figure 1). The system is equipped with two SO110 solid/gas Cs sputter ion sources, each having a 50-position sample carousel. The ion source is operated at a target voltage of –7 kV, an ionizer potential of –28 kV, and with a Cs temperature of 115°C, yielding a total pre-acceleration potential of 35 kV. The ion source is followed by an einzel lens and a 54° electrostatic analyzer (ESA) set to 3.96 kV, which is also used to switch between the two ion sources. Next follows the low-energy (LE) side 120° magnet that is equipped with a Hall probe for feedback control of the magnet field. It is set to 176.5 mT for mass 13 AMU. The LE magnet chamber is set on different bias voltages (2900 V, 0 V, and –2475 V) for fast switching (bouncing) between the masses 12, 13, and 14 AMU. The stable isotopes are injected for 100 µs, while the rare isotope is injected for 9.75 ms, using most of the injection time. After the LE magnet follows the LE einzel lens and the Tandetron accelerator operating at 1 MV for C^{+2} analysis. For carbon AMS analysis, we use argon stripper gas at an inlet pressure of 3E-2 mBar. The high-energy (HE) side 90° analyzing magnet is set to 588.0 mT and separates the $^{12}C^{+2}$, $^{13}C^{+2}$, and $^{14}C^{+2}$ ion beams, where after $^{12}C^{+2}$ and $^{13}C^{+2}$ are measured in two offset Faraday cups. $^{14}C^{+2}$ continues through the rare-isotope (RI) beam line, featuring a 120° ESA followed by a 30° magnet set to 577.5 mT before detection. The detector system features a gas-filled ionization chamber with a $10 \times 10\,mm^2$ entrance window and two anodes for $\Delta E - E_{res}$ measurements (Figure 4C). The chamber is filled with isobutane and is operated at 5.5 mBar.

RESULTS AND DISCUSSION

We have selected charge state +2 for ^{14}C analysis as an alternative to charge state +1. The maximum yield with charge state +2 is obtained at 1MV acceleration voltage and surpasses

*Corresponding author: jesper.olsen@phys.au.dk.

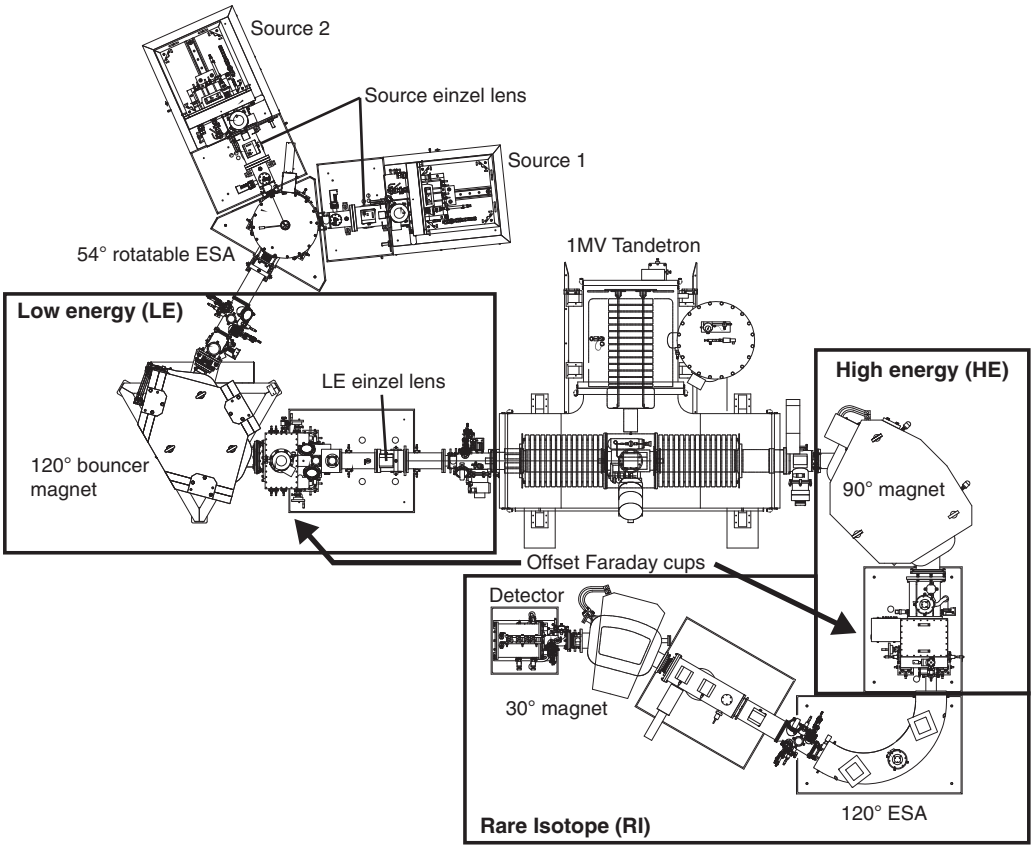

Figure 1 Schematic layout of the 1MV HVE Tandetron accelerator at Aarhus University

the yield for charge state 1+, where the maximum yield is obtained at 0.5 MV (Sung et al. 2015). However, we will in the near future test and report on the performance of charge state +1 on our AMS system.

Initial tests showed that our existing graphitization system produced graphite of too poor quality for AMS ^{14}C analysis on the new accelerator. The major problem with the existing graphitization system was the oven design, resulting in temperature differences between reactors of up to 100°C. Hence, an effort was made to design ovens that could provide constant and uniform temperatures for all reactors. Furthermore, the initial tests showed too high Li isobaric interference (e.g. Hong et al. 2010; Heinemeier et al. 2015; Nadeau et al. 2015).

New Graphitization System

The new graphitization system is constructed using Swagelok VCR components and Swagelok diaphragm valves (DP series) to minimize the use of O-rings and valve dead volume (Figure 2). Where possible, larger parts of the system are welded together to minimize the risk of leaks. The system is equipped with two scroll pumps (Edwards, NXDS10), one for rough evacuation and one to back the turbopump (Edwards, NXDS6). The vacuum system is further equipped with two pneumatic valves for automatic switching between low and high vacuum. The pressure is measured using a wide-range Pirani pressure gauge. Connections to glassware make use of Swagelok Ultra

https://doi.org/10.1017/RDC.2016.85 Published online by Cambridge University Press

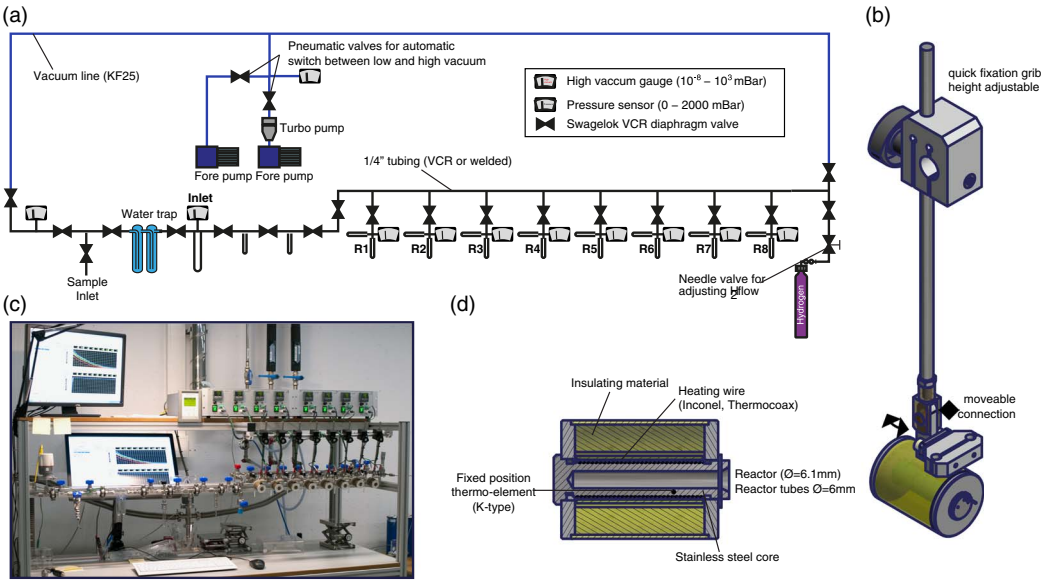

Figure 2 (A) Schematic layout of the graphitization system; (B) mounting arm for graphitization oven; (C) graphitization oven; (D) photo of the AARAMS graphitization system.

Torr fittings. The overall pressure in the graphitization system when idle is below 1E-4 mBar. During operation, the inlet section can be pumped to ~1E-3 mBar, whereas graphitization reactors can be pumped to below 4.5E-5 mBar. Sample size and reactor pressures are measured using AMSYS (5812) pressure transducers connected to a National Instruments module 9205. The reactor ovens are made of boron-nitride and stainless steel with an Inconel heating wire. Oven temperatures are controlled using Eurotherm 3216 temperature controllers built into a homemade electronic box also providing power. The graphitization system is controlled by a LabView program where also pressure time series of the graphitization reaction are recorded (Figure 2).

CO_2 for graphitization is admitted through the inlet port and is cryogenically purified using ethanol cooled with liquid nitrogen to a temperature of –80 to –90°C. The sample yield is measured, then a maximum of 1.1 mg C is transferred cryogenically to the reactor (6 × 50 mm culture tube). If the original sample is larger, it is either chopped or partially discarded. The CO_2 is then reduced using hydrogen in excess (2.1 × CO_2 pressure) with Fe (~2.5 mg) as a catalyst (Vogel et al. 1984, 1987) at 550°C for 4 hr. $Mg(ClO_4)_2$ is used to trap water and is replaced for every second batch (Santos et al. 2004). The graphitization yield is calculated as final reactor pressure divided by the initial reactor pressure; samples with a yield lower than 90% are discarded. Prior to graphitization, the Fe catalyst is reduced using 400 mBar hydrogen at 400°C for 1 hr. Traditionally, quartz glass reactors have been used due to their higher melting point. However, initial tests showed occasionally very high Li counts in the AMS detector. For this reason, we now use reactors of BSi (Pyrex) glass, which appears to yield much lower Li concentrations in the produced graphite (Loyd et al. 1991).

The graphitization system has proven to produce homogeneous graphite yielding a ~25 µA $^{12}C^{+2}$ beam in the accelerator. The graphitization system produces $^{14}C/^{12}C$ background levels well below 5E-15 for various materials (Figure 3). The average ^{14}C age of our standard whale bone pretreated to collagen is 45,170 ± 3170 ^{14}C yr calculated as the mean and standard

https://doi.org/10.1017/RDC.2016.85 Published online by Cambridge University Press

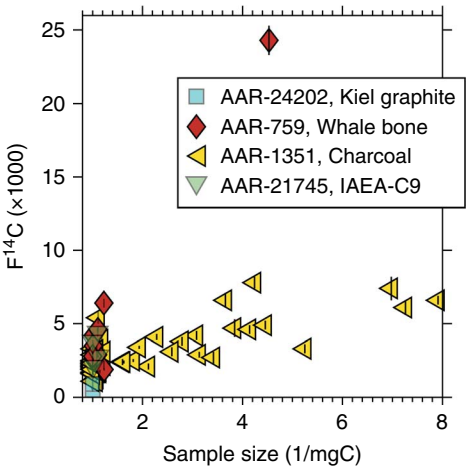

Figure 3 Size plot of various background materials measured between September 2015 and January 2016. Whale bone (collagen, AAR-759) ^{14}C age = 45,172 ± 3170, $F^{14}C$ = 0.0036 ± 0.0014 (n = 9). Charcoal (ABA, AAR-1351) ^{14}C age = 49,016 ± 3124, $F^{14}C$ = 0.0022 ± 0.0009 (n = 51). IAEA-C9 (cellulose, AAR-21745) ^{14}C age = 45,960 ± 2512, $F^{14}C$ = 0.0033 ± 0.0010 (n = 4). Unprocessed graphite (Kiel graphite, AAR-24202) ^{14}C age = 58,647 ± 2032, $F^{14}C$ = 0.0007 ± 0.002 (n = 4).

deviation of samples larger than 0.7 mg C, whereas our charcoal background (ABA) provides an average ^{14}C age of 49,000 ± 3124 ^{14}C yr. The kauri wood background (cellulose) yielded 45,960 ± 2512 ^{14}C yr. The machine background is determined using unprocessed graphite, which yielded 58,650 ± 2032 ^{14}C yr.

$^{7}Li^{+1}$ Interference

Suppression of the isobaric interference from $^{7}Li_2$ is very important for ^{14}C measurements at charge state 2+ (e.g. Hong et al. 2010; Nadeau et al. 2015). Hence, we put some effort in optimizing the system settings in order to decrease the number of Li ions reaching the detector. The ^{12}C transmission through the accelerator has been optimized by scanning the stripper gas pressure. Maximum transmission of ^{12}C (T-12) of 55% was observed at a stripper gas pressure of 1.5E-2 mBar (Figure 4A). However, at this low argon pressure, the breakup of ^{13}CH and $^{7}Li_2$ molecules was not sufficient for the required measurement background. Therefore, we increased the stripper gas pressure to 3.0E-2 mBar to ensure an effective breakup of these molecules in the stripper canal, resulting in a slight decrease of the ^{12}C transmission to 54%. Also, the isobutane detector pressure was varied to ensure maximum isobar separation. With falling detector gas pressure, the ion path gets longer and more energy is deposited at the second anode (E_{res}). Once the pressure becomes too low, the ions are no longer stopped within the sensitive area and both energy signals drop. Thus, the optimal operating pressure is when the energy is deposited approximately equally in both anodes. The optimal detector gas pressure was found to be 5.5 mBar (Figure 4B–C).

Lithium ions can reach the detector when produced in the ion source as dimer $^{7}Li_2^-$ and subsequent molecule disassociation in the stripper canal, forming two single $^{7}Li^+$ ions. Because of

https://doi.org/10.1017/RDC.2016.85 Published online by Cambridge University Press

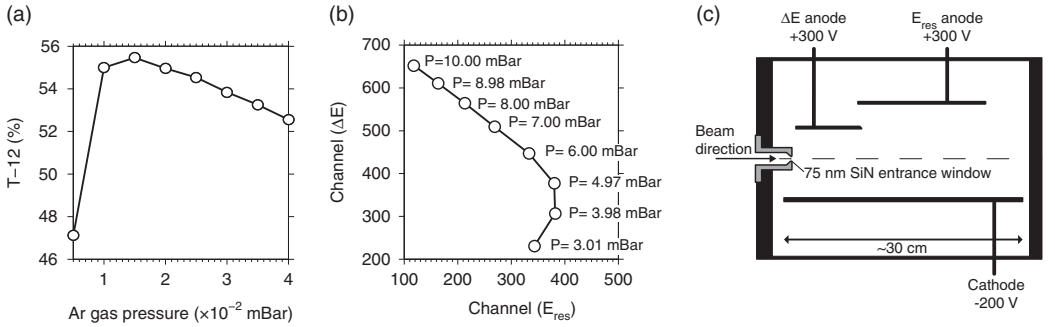

Figure 4 (A) Scanning profile of the carbon transmission (obtained as the measured $^{12}C^{+2}$ current divided by the injected $^{12}C^{-}$ current times one-half to take into account the charge state) as a function of the argon stripper pressure. (B) Optimization of the detector gas pressure. The isobutane pressure is varied from 3 to 10 mBar and the $^{14}C^{+2}$ peak centers are plotted. (C) Schematic layout of the gas ionization detector.

energy and momentum conservation, the two ^{7}Li ions produced in the breakup of $^{7}Li_2^-$ molecules will equally share the energy of the original $^{7}Li_2$ molecule. Hence, $^{7}Li^{+1}$ will have half the energy of a $^{14}C^{+2}$ ion at the exit of the accelerator. The electrostatic rigidity of the $^{7}Li^{+1}$ ion and the $^{14}C^{+2}$ ion will thus be equal, but the magnetic rigidity of the $^{7}Li^{+1}$ ion and the $^{14}C^{+2}$ ion will be different because of the small mass difference per nucleon between ^{7}Li (atomic weight 7.016) and ^{14}C (atomic weight 14.003). However, the HE magnet mass resolution is not large enough to completely separate $^{7}Li^{+1}$ from $^{14}C^{+2}$. Nonetheless, the bending radius of the $^{7}Li^{+1}$ ion beam will be slightly larger than the $^{14}C^{+2}$ bending radius and the $^{7}Li^{+1}$ ion beam will therefore be positioned at the outer side of the reference path. This fact can be exploited to suppress the $^{7}Li^{+1}$ ion beam significantly (Hong et al. 2010). Furthermore, our AMS system is equipped with a 30° magnet (RI magnet) just before the detector, which potentially may help reduce the $^{7}Li^{+1}$ ion beam further. It should be noted here that only if both of the Li^{+1} molecule fragments reach the detector, the resulting event comes close to the ^{14}C region of interest. If one Li is stopped, the detector registers only half of the energy, which is clearly separated from ^{14}C (Figures 5C–E). In the detector spectra, the peak in the lower left corner is $^{7}Li^{+1}$, whereas the peak in the upper-right corner close to the ^{14}C region is caused by two coinciding $^{7}Li^{+1}$ ions. In itself, the $^{7}Li^{+1}$ peak is well separated from the ^{14}C peak. It is only when both $^{7}Li^{+1}$ ions reach the detector that $^{7}Li^{+1}$ imposes a serious threat against obtaining accurate ^{14}C counts.

An experiment to minimize ^{7}Li interference made use of both the RI ESA and RI magnet. For comparison, we examined a sample heavily contaminated with Li and a sample that previously showed very low Li counts in the detector. In the first experiment, the RI magnet was set to the midpoint of the magnetic field profile, allowing ^{14}C to reach the detector and the RI ESA electric field was scanned (Figure 5A). Figure 4C shows the spectrum at peaking Li interference (V_{ESA} = 58.79 kV, and RI magnet at 87.5A), while Figure 4D shows a spectrum at a higher ESA setting (V_{ESA} = 58.9 kV), where ^{14}C is still fully transmitted but the Li interference is drastically reduced. Clearly, the RI ESA midpoint value of 58.79 kV cannot be used without compromising the ^{14}C counts, whereas an RI-ESA electric field value at 58.90 kV substantially reduces the $^{7}Li^{+1}$ counts. Coincident $^{7}Li^{+1}$ counts are completely removed at this setting (Figure 5D).

A similar experiment is conducted by scanning the RI magnet field with the RI ESA set at the midpoint value (58.79 kV, Figure 5B). When a higher than midpoint RI magnet field value is chosen, the $^{7}Li^{+1}$ ions are significantly suppressed even though $^{7}Li^{+1}$ coincidence counts are

https://doi.org/10.1017/RDC.2016.85 Published online by Cambridge University Press

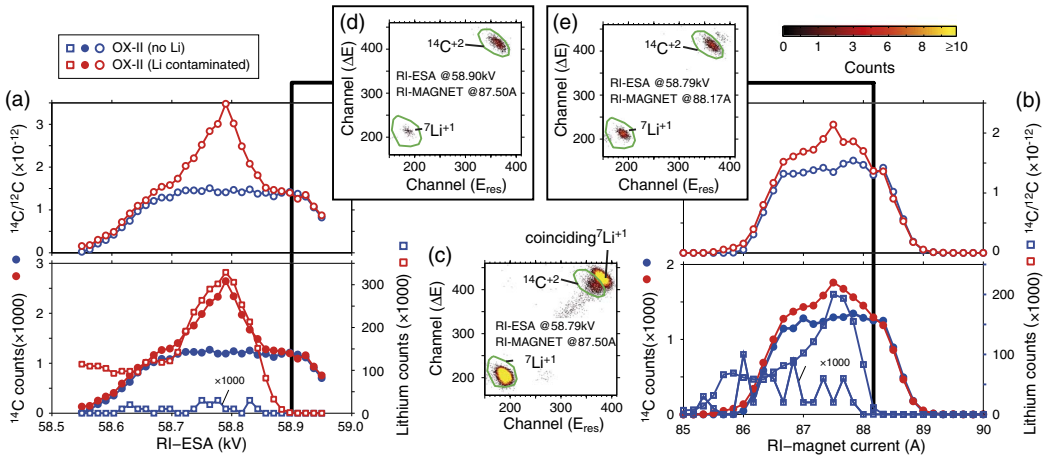

Figure 5 Tuning of rare-isotope electrostatic analyzer (RI ESA) and rare-isotope (RI) magnet to avoid Li interference using a clean and Li contaminated OX-II sample. (A) Tuning profile of the RI-ESA. (B) Tuning profile of the BI magnet. Shown in both (A) and (B) are the ^{14}C counts, Li counts, and the $^{14}C/^{12}C$ ratio. (C) Detector spectrum from a heavily Li contaminated sample acquired with both the RI ESA and RI magnet at their midpoint setting. (D) Detector spectrum from a heavily Li contaminated sample acquired with the optimal RI ESA setting. (E) Detector spectrum from a heavily Li contaminated sample acquired with the optimal RI magnet setting.

still visible (Figure 5E). Offsetting both the RI ESA and RI magnet significantly reduced the $^{7}Li^{+1}$ counts for a sample heavily contaminated with Li from above 300,000 to well below 100. Because of the field control of the RI magnet and because the ion beam position is reproducible within 0.1 mm at the entrance of the RI ESA due to slit stabilization of the $^{13}C^{+2}$ ion beam in the HE offset Faraday cup, the settings reported here have been found to be stable over time. Since August 2015, we have not experienced problems with Li during ^{14}C analysis. Prior to this period, Li interference was a serious problem for about 5% of all samples. To further decrease the $^{7}Li^{+1}$ ion beam, the X-slit at the entrance to the RI ESA is narrowed.

Current Dependencies of the Transmission of ^{12}C

Steerers, analyzers, and other beam-guiding components are flat-top tuned for maximum sensitivity and their settings show no dependency on the source output current. This, however, is not the case for the source and LE einzel lenses, for which the optimal settings do depend on the current (Figures 6A–B). To minimize this effect, we adjust the electric potential of both the source and BI einzel lens to a midpoint value for the expected beam currents. Consequently, we divide our measurement batches into normal-sized (>0.5 mg C) and small-sized samples (<0.5 mg C). Further, we produce all standards to match the sample sizes present in any batch. We use OX-II as our primary standard and add at least two secondary standards to each batch. As a result, we can correct the $^{13}C/^{12}C$ and $^{14}C/^{12}C$ data for the output current, as the dependencies are typically linear.

Figure 6A–B show scanning profiles taken over the last 6 months at different currents and different machine settings, which are remarkably consistent. It can be noticed that the optimum point of each profile is a linear function of the $^{12}C^{+2}$ current. This linear dependency of the einzel lens electrostatic potential as a function $^{12}C^{+2}$ current can be used to predict the optimal source and LE lenses' electrostatic potential by measuring the $^{12}C^{+2}$ current. Figures 5C–F show data from a routine batch where both einzel lenses were set according to the best possible

https://doi.org/10.1017/RDC.2016.85 Published online by Cambridge University Press

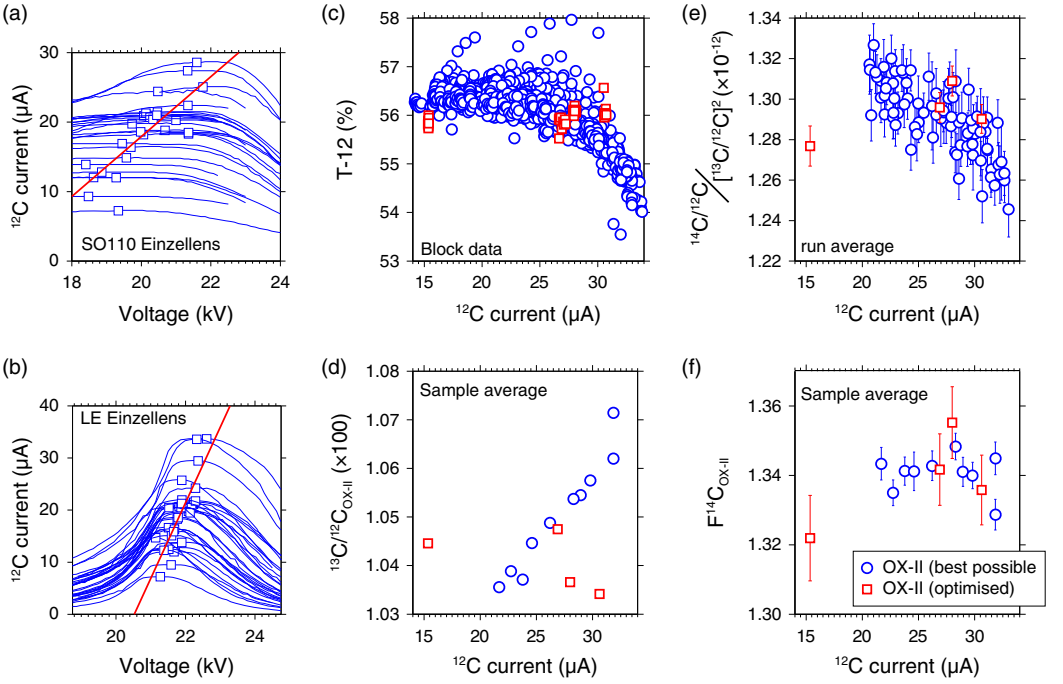

Figure 6 Source einzel lens scanning profiles of the $^{12}C^{+2}$ current acquired during tuning of the accelerator in the period from August 2015 to February 2016. (B) LE einzel lens profiles of the $^{12}C^{+2}$ current acquired during tuning of the accelerator in period from August 2015 to February 2016. For both (A) and (B), the squared points denote the flat-top midpoint of the profile. The red line (refer to online version for color references) is a linear fit to the flat-top midpoints. (C) The T-12 transmission ($0.5 \times {}^{12}C^{+2}/{}^{12}C^{-1}$) as a function of the $^{12}C^{+2}$ current. Blue circles are the transmission value of all block (about 8 blocks constitutes one run) measurements during a routine analysis. (D) The $^{12}C^{+2}$ current as a function of the sample (about 8 runs constitute one sample average) averaged $^{13}C/^{12}C_{OX-II}$ ratio. (E) The $^{12}C^{+2}$ current as a function of the run averaged fractionation-corrected $^{14}C/^{12}C_{OX-II}$ ratio (for calculation details, please consult Steier et al. 2004). (F) $F^{14}C_{OX-II}$ as a function of the $^{12}C^{+2}$ current. (D–F) Blue circles denote OX-II values acquired during normal routine operation of the AMS system. (C–F) Red squared points are OX-II test samples acquired with the optimal flat-top setting of both the source and BI einzel lenses.

compromise with respect to the expected source yield of the samples. Using these optimized, but fixed, settings results still in a current dependency of the ^{12}C transmission. In particular, currents higher than 25 μA appear to be affected, most probably due to larger space-charge effects at higher beam intensities with a loss of ^{12}C beam through the accelerator as a consequence. Similarly, both the $^{13}C/^{12}C$ ratio as well as the fractionation-corrected $^{14}C/^{12}C$ ratios depend on the beam current.

A test to remove this current dependency by adjusting the lens settings used four cathodes of different size. Before running each cathode, the source and BI einzel lens electrostatic potential was set according to a linear fit to the profile top points (Figure 6). With the optimized source and LE einzel lenses, the transmission becomes more or less independent of the $^{12}C^{+2}$ current. Furthermore, the $^{13}C/^{12}C$ ratios and the fractionation-corrected $^{14}C/^{12}C$ ratios show much more constant values when plotted versus the $^{12}C^{+2}$ current. This makes it a promising idea to eliminate the current dependencies of the analysis results by automatically adjusting the source and LE einzel lens determined by the measured $^{12}C^{+2}$ current. We are currently in contact with HVE about possibilities for changing the measurement method accordingly.

https://doi.org/10.1017/RDC.2016.85 Published online by Cambridge University Press

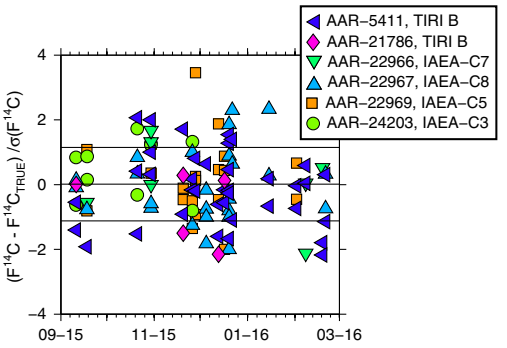

Figure 7 Time series of international standards covering the period from September 2016 to February 2016: (A) TIRI B standard with consensus $F^{14}C = 0.5709$ (Gulliksen and Scott 1995); (B) IAEA-C7 standard with consensus $F^{14}C = 0.4953 \pm 0.0012$ (Le Clercq et al. 1998); (C) TIRI B standard with consensus $F^{14}C = 0.5709$ (Gulliksen and Scott 1995); (D) IAEA-C3 standard with consensus $F^{14}C = 1.2941 \pm 0.0006$ (Rozanski 1992); (E) IAEA-C8 standard with consensus $F^{14}C = 0.1503 \pm 0.0017$ (Le Clercq 1998); (F) IAEA-C5 standard with consensus $F^{14}C = 0.2305 \pm 0.0002$ (Rozanski 1992).

^{14}C Analysis of International Standards

The performance of the ^{14}C system was tested using five different international standards (Figure 7). The TIRI B sample occurs twice as we have two different batches of this standard. All ages are quoted as fraction modern ($F^{14}C$) and corrected for natural fractionation in accordance with Stuiver and Polach (1977). The isotopic fractionation correction is carried out online using $^{13}C/^{12}C$ ratios derived from the AMS analysis. For each of the standards, a weighted mean $F^{14}C$ (μ_w) and standard error (σ_w) is calculated. Sample sizes range from ~0.1 to 1.1 mg C and are all included in the weighted average value. Reduced χ^2 statistics are used to assess if the sample weighted average is normally distributed (Bevington and Robinson 2003). The difference between μ_w is calculated as a z-score $z = (\mu_w - \text{true value})/\sigma_w$. As seen from Figure 7, the majority of the international standards shows z-scores around or less than 1; furthermore, all samples passed the reduced χ^2 statistics. In particular, time series with a large number ($n > 25$) of measurements (AAR-5411 and AAR-22967) show very good agreement with their true values.

CONCLUSION

Progress and performance for ^{14}C analysis on the Aarhus HVE Tandetron AMS have been presented. A challenge when running ^{14}C analysis at charge state 2+ is isobaric interference from Li^{1+}. Hence, an effort to minimize isobaric interference from Li^{1+} has been carried out by optimizing the graphitization procedure. Furthermore, the settings of the high-energy ESA and high-energy 30° second magnet (positioned just before the detector) have been optimized. The machine background is determined using unprocessed graphite to $58{,}650 \pm 2032$ ^{14}C yr. Processed background materials ranged from 45,100 to 49,000 ^{14}C yr. The majority of the international standards agree with their true value within 1.6 standard deviations.

https://doi.org/10.1017/RDC.2016.85 Published online by Cambridge University Press

ACKNOWLEDGMENTS

The laboratory technicians at AARAMS are thanked for their help with preparing targets for ^{14}C analysis. Two anonymous reviewers are thanked for their constructive remarks, which helped us to improve the manuscript.

REFERENCES

Bevington PR, Robinson DK. 2003. *Data Reduction and Error Analysis for the Physical Sciences*. New York: McGraw-Hill.

Gulliksen S, Scott M. 1995. Report of the TIRI workshop, Saturday 13 August 1994. *Radiocarbon* 37(2):820–1.

Heinemeier J, Olsen J, Klein M, Mous D. 2015. The new extended HVE 1 MV multi-element AMS system for low background installed at the Aarhus AMS Dating Centre. *Nuclear Instruments and Methods in Physics Research B* 361:143–8.

Hong W, Park JH, Sung KS, Woo HJ, Kim JK, Choi HW, Kim GD. 2010. A new 1MV AMS facility at KIGAM. *Radiocarbon* 52(2):243–51.

Klein MG, Mous DJW, Gottdang A. 2006. A compact 1 MV multi-element AMS system. *Nuclear Instruments and Methods in Physics Research B* 249(1–2):764–7.

Klein MG, van Staveren HJ, Mous DJW, Gottdang A. 2007. Performance of the compact HVE 1 MV multi-element AMS system. *Nuclear Instruments and Methods in Physics Research B* 259(1):184–7.

Klein MG, Heinemeier J, Gottdang A, Mous DJW, Olsen J. 2014. Extension of the HVE 1 MV multi-element AMS system for low background. *Nuclear Instruments and Methods in Physics Research B* 331:204–8.

Le Clercq M, van der Plicht J, Gröning M. 1998. New ^{14}C reference materials with activities of 15 and 50 pMC. *Radiocarbon* 40(1):295–7.

Loyd DH, Vogel JS, Trumbore S. 1991. Lithium contamination in AMS measurements of ^{14}C. *Radiocarbon* 33(3):297–301.

Nadeau M-J, Vaernes E, Svarva HL, Larsen E, Gulliksen S, Klein M, Mous DJW. 2015. Status of the "new" AMS facility in Trondheim. *Nuclear Instruments and Methods in Physics Research B* 361:149–55.

Rozanski R. 1992. The IAEA ^{14}C Intercomparison Exercise 1990. *Radiocarbon* 34(3):506–19.

Santos GM, Southon JR, Druffel-Rodriguez KC, Griffin S, Mazon M. 2004. Magnesium perchlorate as an alternative water trap in AMS graphite sample preparation: a report on sample preparation at KCCAMS at the University of California, Irvine. *Radiocarbon* 46(1):165–73.

Steier P, Dellinger F, Kutschera W, Priller A, Rom W, Wild EM. 2004. Pushing the precision limit of ^{14}C AMS. *Radiocarbon* 46(1): 5–16.

Stuiver M, Polach HA. 1977. Discussion: reporting of ^{14}C data. *Radiocarbon* 19(3):355–63.

Sung KH, Hong W, Park G, Lee JG. 2015. Radiocarbon measurement with 1 MV AMS at charge state 1. *Nuclear Instruments and Methods in Physics Research B* 361:586–90.

Vogel JS, Southon JR, Nelson DE. 1987. Catalyst and binder effects in the use of filamentous graphite for AMS. *Nuclear Instruments and Methods in Physics Research B* 29(1–2):50–6.

Vogel JS, Southon JR, Nelson DE, Brown TA. 1984. Performance of catalytically condensed carbon for use in accelerator mass spectrometry. *Nuclear Instruments and Methods in Physics Research B* 5(2):289–93.